

CHAPTER 6

Bijels Formed by Solvent Transfer-induced Phase Separation

MARTIN F. HAASE^{*a,b}, STEPHEN BOAKYE-ANSAH^b, GIUSEPPE DI VITANTONIO^c, KATHLEEN J. STEBE^c AND DAEYEON LEE^c

^aVan't Hoff Laboratory for Physical and Colloidal Chemistry, Debye Institute for Nanomaterial Science, Utrecht University, Padualaan 8, Utrecht 3584 CH, The Netherlands; ^bDepartment of Chemical Engineering, Rowan University, 201 Mullica Hill Road, Glassboro, New Jersey 08028, USA;

^cDepartment of Chemical and Biomolecular Engineering, University of Pennsylvania, Philadelphia, PA, 19104, USA

*E-mail: m.f.haase@uu.nl

6.1 Introduction

Two immiscible liquids can mix upon the addition of a co-solvent. This ternary mixture allows for the dispersion of colloidal particles *via* careful tuning of the particle surface chemistry. The mixture can be induced to undergo spinodal decomposition upon removal of the solvent, providing a powerful platform to produce bicontinuous interfacially jammed emulsion gels (bijels) by arresting this phase separation with nanoparticles. This alternative approach for the formation of bijels has been termed ‘solvent transfer-induced phase separation’ (STrIPS).¹ STrIPS represents an innovation in the

field of particle-stabilized biphasic liquid mixtures by introducing a scalable and continuous route for the production of bijel microparticles, fibers or planar films with remarkable potential applications. STrIPS bijels have been used to form hollow-fiber membranes for ultrafiltration,² and have enabled biphasic reactive separations.³

In this chapter, we provide an overview of the current state of research on STrIPS bijels, by (1) introducing ternary liquid phase separation, (2) detailing basic principles of STrIPS bijel formation, (3) highlighting applications, and (4) providing an outlook for future directions of these innovative materials.

Section 6.2 discusses the basis for STrIPS, the ternary liquid–liquid phase diagram. Thereafter, the origins of STrIPS for the formation of multiple emulsions by ternary liquid–liquid phase separation are discussed.⁴ Section 6.3 introduces the impact of nanoparticle addition to the ternary liquid mixture, a critical step for bijel formation *via* STrIPS. We detail the formation of bijels *via* STrIPS by highlighting the dependencies of bijel morphology on fabrication parameters. We show how the selection of monomer-containing oil phases facilitates the formation of nanoparticle-coated polymer scaffolds, which provide additional insight into the dynamic processes during STrIPS. Moreover, we discuss the yield/fracture strength of the phase-separating mixture and detail the mechanical properties of STrIPS bijels.⁵ Sections 6.4 and 6.5 focus on applications for STrIPS bijels. We first show how the bicontinuous liquid scaffold of STrIPS bijels can be used for the biphasic synthesis of chemicals *via* reactive catalytic separations. To realize this potential, a chemical reinforcement approach for bijels is introduced. Furthermore, we show how a modified extrusion technique combined with the selective polymerization of the oil scaffold of the bijel enables the formation of hollow-fiber membranes for ultrafiltration applications with a biofouling-resistant membrane surface. Moreover, this technique is used to template pH-responsive hydrogel scaffolds with potential biomedical applications.

6.2 Basic Principles of Solvent Transfer-induced Phase Separation

6.2.1 Ternary Phase Diagrams

Ternary liquid mixtures are important for industrial separation processes, but also for some alcoholic drinks. Diluting the Greek spirit ouzo in a glass of water produces a mixture with a milky appearance (Figure 6.1a). Known as the ‘ouzo effect’,⁶ remarkably uniform and stable microscopic droplets form by nucleation of anethole, a liquorice-like ingredient in ouzo. The ternary mixture system ouzo is made of ethanol (~40–50 vol%), water (~50 vol%) and anethole (remaining volume). During dilution in water, the homogeneous mixture crosses the binodal line in the ternary diagram to undergo droplet nucleation, as depicted in Figure 6.1b. Ternary liquid–liquid equilibria are

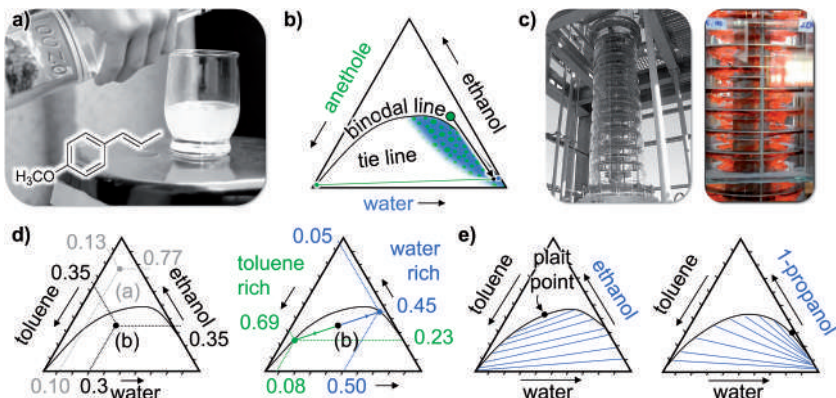


Figure 6.1 Solvent partitioning in ternary mixtures. (a) Photograph of ouzo dilution in water. (b) Ternary liquid phase diagram depicting the compositional path for mixing ouzo with water. (c) Photographs of rotating disc extractors, with orange droplets rising in the extraction apparatus, (d) Ternary phase diagrams, exemplifying the compositions of water-rich and monomer-rich phases, connected by a tie-line. (e) Effect of decreasing solvent polarity on the tie-line slope. All phase diagrams are given in volume fractions.

also used by chemical engineers to design liquid–liquid extraction-based separations. Typically, a solute is enriched (purified) in liquid A and depleted in a second immiscible liquid, B. The mass transfer of the solute is enhanced by strong shear stresses and increased interfacial area, generated, for instance, in rotating disc extractors, as shown in Figure 6.1c.

To illustrate the use of the ternary phase diagram in understanding the behavior of ternary mixtures of oil–water–(co-)solvent, we use the triangular diagram of toluene–ethanol–water mixture as an example, as shown in Figure 6.1d. Point (a) is in the monophasic region and contains 77% ethanol, enough to mix 13% of toluene with 10% of water. In contrast, point (b) is in the biphasic region, which contains 35% ethanol, which is insufficient to mix 35% of toluene with 30% of water. As a result, point (b) splits along a tie-line into two new ternary mixtures, one rich in toluene (left) and the other rich in water (right). The tie-lines converge at the plait point of the ternary diagram (Figure 6.1e). The mass/volume ratio of the two phases can be determined using the lever rule. The location of the plait point (*i.e.*, left or right half of the triangle) determines the slope of the tie-lines, and thereby the partitioning behavior of the solvent. For instance, the tie-lines for ethanol are tilted upwards, indicating that the water-rich phase always contains more ethanol than the toluene-rich phase (Figure 6.1e, left). In contrast, for 1-propanol the tie-lines are tilted downwards, and the oil-rich phase contains more 1-propanol than the water-rich phase. These basics provide valuable guidance to understand the complexity of solvent partitioning during STrIPS, a process that was initially investigated for the microfluidic formation of multiple emulsion droplets, as discussed in the following section.

6.2.2 Microfluidic Control of Solvent Transfer-induced Phase Separation

Phase separation is triggered by injecting a homogeneous ternary mixture of oil, water and solvent into water (Figure 6.2a).^{4,7–10} To this end, a coaxial extrusion device composed of two centered glass capillaries is connected *via* tubing to syringe pumps that continuously flow both ternary mixture and water into the device. Droplets of the ternary mixture form at the coaxial nozzle, pinch-off periodically and are transported downstream by the water. During this process, solvent diffuses to the water stream and demixing takes place within the droplet, giving the technique its name ‘solvent transfer-induced phase separation’ (STrIPS).

STrIPS is depicted in the ternary phase diagram of Figure 6.2b. The ternary mixture (1) is prepared so as to have a composition close to the plait point. Transfer of solvent to the water stream shifts the ternary composition into the immiscible region. The mass transfer rate is maximized with a solvent of preferential partitioning to water, for instance, methanol or ethanol. After splitting into two phases, ongoing solvent transfer to the large volume of water results in roughly pure oil and water, located in the lower right and left corners of the diagram.

Phase separation during STrIPS proceeds either *via* nucleation and coalescence, or *via* spinodal decomposition. Figure 6.2c shows a time series of a droplet with the initial composition of point (2) undergoing demixing (top row). Five seconds after droplet formation, the droplet strongly scatters light, indicating nucleation of water droplets; after 11 seconds, coalescing water droplets are observed that merge to form a single large water droplet in the center at 13 seconds. In contrast, a droplet with composition 1 shows significantly less light scattering at 5 seconds,

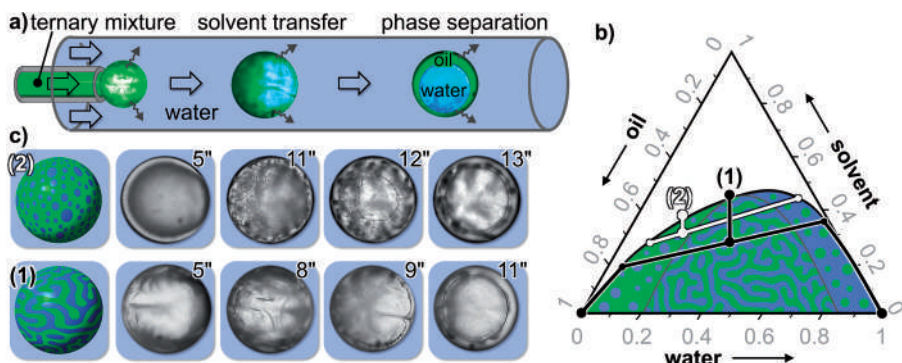


Figure 6.2 STrIPS. (a) Schematics of microfluidic device with false-color micrographs of droplets undergoing STrIPS. (b) Ternary phase diagram with two different starting compositions. (c) Micrograph time series of droplets with the two different initial compositions resulting in nucleation (composition 2) *versus* spinodal decomposition (composition 1).

and demixing results in the abrupt formation of a central water droplet without the appearance of coalescing droplets at 11 seconds (Figure 6.2c, bottom row). The difference in the droplet morphology of composition 1 is due to gradual coarsening of domains *via* spinodal decomposition, which eliminates sudden formation of small internal droplets that strongly scatter light.

The control of the type of phase separation by the initial ternary mixture composition inspires the use of STrIPS to produce bijels. To this end, it is necessary to disperse surface-active nanoparticles within the ternary mixture, as we discuss in the following section.

6.3 Bijel Formation by STrIPS

6.3.1 Dispersing Surface-active Nanoparticles in the Ternary Mixture

Silica nanoparticles can be readily dispersed in water over a broad range of pH values. However, the solvent environment in the ternary liquid mixtures does not facilitate particle dispersion. This can be related to incompatibility between the hydrophilic silica surface and the hydrophobic constituents of the ternary mixture. To enable dispersion, surface modification of silica particles is imperative.

In situ modification of silica nanoparticles *via* electrostatic interactions with alkyltrimethylammonium cations (ATACs), as depicted in Figure 6.3a, has proven to be a powerful approach to modify the silica surface. For particle dispersion, the amount of adsorbed ATACs needs to be controlled to facilitate compatibility between the silica particles and the ternary mixture. Control over the adsorbed amount is possible *via* (1) the

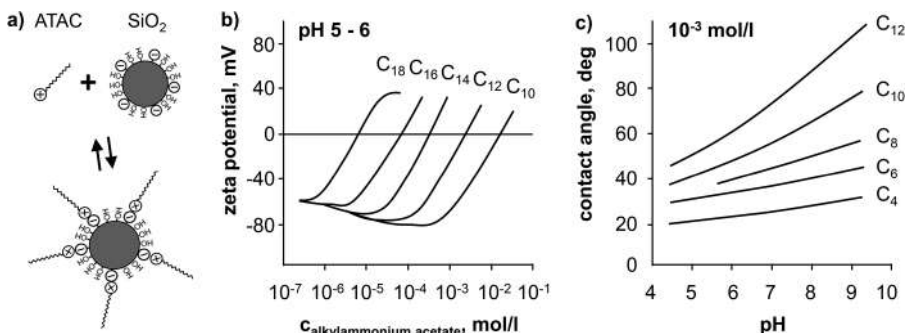


Figure 6.3 Surface modification of silica by alkylammonium cations. (a) Simplified schematic of ATAC adsorption on silica particles. (b) Dependence of zeta potentials of silica particles on the concentrations of alkylammonium cations of different chain lengths. (c) Dependence of contact angle of a water droplet containing 1 mM of alkylammonium cations of different chain lengths on a planar silica surface under hexane on the pH value.

ATAC concentration, (2) the ATAC chain length and (3) the surface charge density of the silica.^{11,12} Figure 6.3b shows how the zeta potential of silica particles changes with increasing adsorption of ATACs in water. Both concentration and chain length increase the adsorbed amount, reducing the negative charge of the silica surface. Moreover, sufficiently high ATAC concentrations cause charge reversal of the surface, suggesting formation of ATAC double layers on the silica surface.^{13,14} Figure 6.3c shows how the contact angle of a droplet of an aqueous ATAC solution in hexane on a silica surface increases with the pH value at a fixed ATAC concentration of 1 mM.¹⁵ The adsorption of the ATACs renders the surface partially hydrophobic due to surface coating with alkyl chains. High pH values and long alkyl chains increase the contact angle. However, at low pH values, the low surface charge density of the silica reduces the ATAC adsorption.

The moderation of the ATAC adsorption *via* the solution pH presents an opportunity for dispersing silica particles in the ternary mixture. Silica nanoparticles (Ludox TMA) in aqueous media at pH 3 can be readily dispersed at high weight fractions (10–40 wt%) in the ternary mixture with hexadecyltrimethylammonium bromide (CTAB) at concentrations ranging from 24 to 80 mmol l⁻¹. In contrast, the same particles at pH values above 5 cannot be dispersed in the mixture at any CTAB concentration. However, the exact mechanism of particle dispersion in the ternary mixture is still subject to current investigation.

Extrusion of the ternary mixture made of oil–water–ethanol with CTAB-modified silica nanoparticles results in a remarkably different behavior compared with the extrusion of the particle-free liquid ternary mixture, as discussed in Section 6.3.2.

6.3.2 STrIPS With *In Situ* Surfactant Nanoparticle Modification

Figure 6.4a shows the ternary phase diagram depicting regions of binodal and spinodal phase separation. In Figure 6.4b the droplet pinch-off for the pure ternary liquid mixture composition 5 is presented (Figure 6.4a).¹ Spherical droplets with spinodal patterns resulting from solvent transfer into the surrounding water are formed. The droplet pinch-off behavior changes dramatically when CTAB and silica nanoparticles (~20 nm diameter, Ludox TMA) are added to mixture 5 (Figure 6.4c). The phase-separating mixture behaves like a viscoelastic material, with non-spherical droplets pinching off from the nozzle. These droplets retain their shape when collected on a microscope slide.

Surface treatment of glass capillary with poly (diallyldimethylammonium chloride) (PDADMAC) enables continuous extrusion of a uniform fiber, as shown in Figure 6.4d, which continues to undergo coarsening that is eventually arrested due to interfacial attachment and jamming of silica nanoparticles at the oil–water interface (see schematics in Figure 6.4a). The fiber undulates into a helical coil when exiting the microfluidic device into a water-filled vial (Figure 6.4e). The structure of the resulting fibers can be characterized by confocal laser-scanning microscopy after collection.

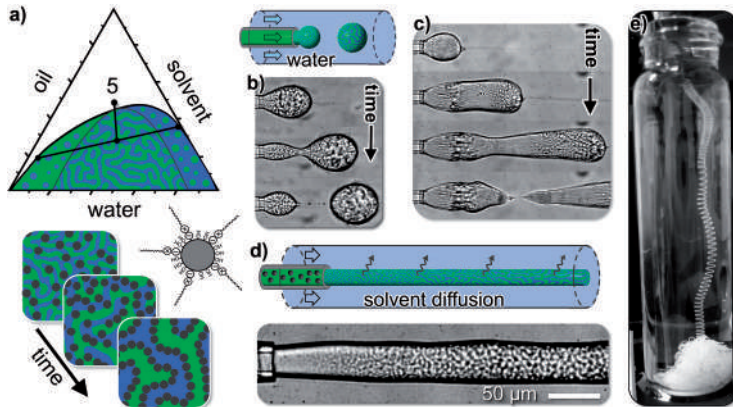


Figure 6.4 Combination of STrIPS and interfacial jamming. (a) Ternary diagram and schematics of interfacial jamming. Microfluidic extrusion of (b) pure ternary mixture and (c) CTAB- and silica-doped ternary mixture. (d) and (e) Micrographs and photographs of continuous fiber extrusion. Adapted from ref. 1 with permission from John Wiley and Sons, © 2015 WILEY-VCH Verlag GmbH & Co. KGaA, Weinheim.

Figure 6.5a shows three-dimensional (3D) reconstructions of z-stacks obtained by confocal microscopy. The arrested cylindrical morphology indicates that the liquid oil/water mixture within the fibers is stabilized by the CTAB-modified nanoparticles. Furthermore, the interpenetrating channel-like structure on the fiber surface shows that spinodal phase separation was arrested. Increasing both CTAB and nanoparticle concentrations results in smaller domain sizes of the bicontinuous channels on the fiber surface. Higher nanoparticle concentrations induce an earlier arrest of phase separation by interfacial jamming, resulting in decreased domain sizes. Increasing the CTAB concentration likely renders the nanoparticles more surface active, explaining the domain size dependence on the CTAB concentration. Surface domain sizes as small as 400 nm were found for compositions with 108 mM CTAB and 4 vol% silica nanoparticles.

The high refractive index (RI) of the oil phase diethyl phthalate (DEP) (RI 1.499) results in low bijel transparency, and low scanning visibility of the internal structures. The transparency, however, can be drastically enhanced upon replacing DEP with the lower refractive index oil hexane-dioldiacrylate (HDA, RI 1.45) and upon adding 20 vol% glycerol to the water phase (Figure 6.5b).

The confocal z-stack of a fiber made with HDA, and the fluorescent dyes Nile red in HDA (false colored in green) and fluorescein sodium salt in water (false colored in blue), reveals that STrIPS bijel fibers have asymmetric morphologies. The domains on the surface (2–5 µm) are significantly smaller than those found in the interior (20–30 µm). Such a gradient in the radial pore size is the unique characteristic of STrIPS bijels. Small domains on the surface likely develop due to the rapid solvent removal to the surrounding

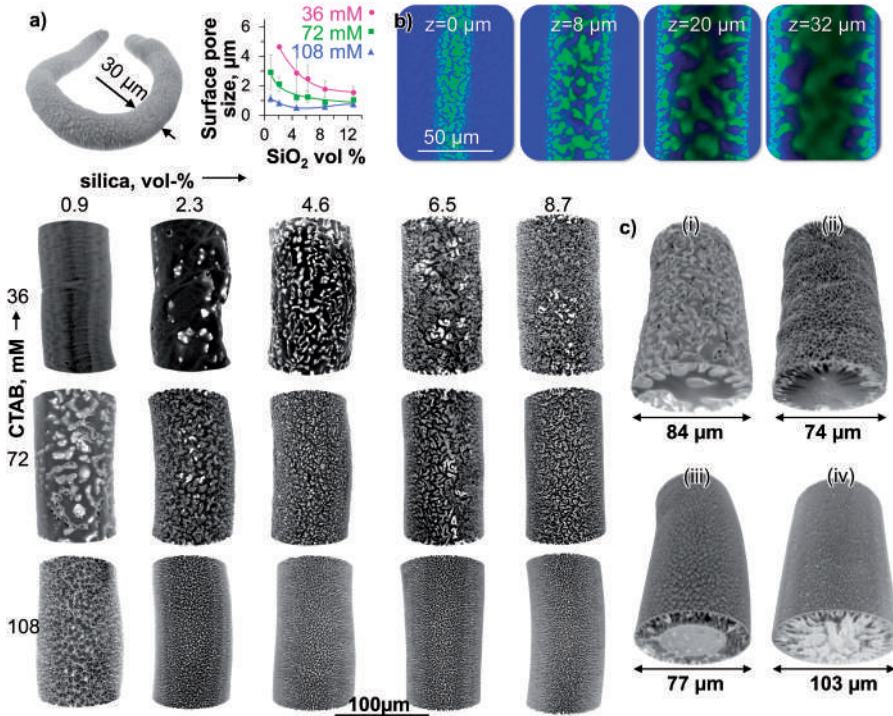


Figure 6.5 Confocal microscopy characterization of STriPS bijels. (a) 3D confocal laser-scanning microscopy reconstructions of bijel fibers and microparticles. (b) Confocal microscopy z-stack of surface and internal structures of a bijel fiber. (c) 3D confocal microscopy reconstructions of bijel fibers fabricated at different CTAB and silica mass fractions. Adapted from ref. 1 with permission from John Wiley and Sons, © 2015 WILEY-VCH Verlag GmbH & Co. KGaA, Weinheim.

water, which results in pure oil and water phases with high surface tensions, enabling strong interfacial particle attachment and jamming. In contrast, the internal domains of the bijels experience a delay in solvent transfer. As a result, the oil- and water-rich phases contain significant amounts of ethanol for prolonged periods of time. This likely results in extended coarsening periods of the phase-separated domains, since the corresponding low surface tensions do not enable efficient interfacial jamming.

To obtain 3D confocal reconstructions of high quality, bijel fibers prepared with HDA need to be polymerized. The polymerized fibers are submerged in diethyl phthalate (after water removal by ethanol) to obtain highly transparent, refractive index-matched fibers. 3D reconstructions of confocal microscopy z-stacks of these specimens are shown in Figure 6.5c.

STriPS-based formation of bijels results in a collection of diverse structures, which can be controlled by changing the concentrations of CTAB and silica, as well as the composition of the initial ternary mixture, as shown

in Figure 6.5c. Nodular structures with large domains (Figure 6.5c(i)) are obtained when the initial compositions of ternary mixtures are close to the critical point and the concentrations of silica and CTAB are kept low (*i.e.*, 1–3 vol%, 30–40 mM). Hollow fibers (Figure 6.5c(iii)) are obtained for intermediate silica and CTAB concentrations (4–5 vol%, 40–70 mM), and fibers with submicrometer surface domains and strong radial alignment of the internal structures (Figure 6.5c(iv)) are obtained for high silica and CTAB concentrations (5–9 vol%, 70–110 mM).

SEM images of polymerized STRIPS bijels reveal the interfacially jammed nanoparticles on the bijel. Figure 6.6a shows a magnified perspective of the bijel surface, revealing a network of bicontinuous channels. Magnification of this perspective shows that the surface of the channels is coated with a packed film of silica nanoparticles.

Figure 6.6b shows electron micrographs of polymerized bijels formed with different ethanol concentrations in the water stream. The ternary mixture for these samples includes high silica contents (>6.5 vol%). With 0% ethanol in the water stream, the fibers do not show characteristic bicontinuous surface channels. Instead, the entire surface is coated by a densely packed film of silica nanoparticles. The effective surface pore size of these fibers is given by the interstitial space between the particles (~5 nm). We will show later that these fibers can be utilized as ultrafiltration membranes (see Section 6.5.3). When the water stream contains 5 vol% ethanol, some micrometer-sized surface domains appear. When the concentration of ethanol in the external water phase is further increased to 10 vol%, the surface pores become larger in size until 20 vol% ethanol, at which point the entire fiber surface is made of bicontinuous oil/water channels.

A possible explanation for this trend is the moderation of the silica particle aggregation by ethanol. Although the particles disperse well in the

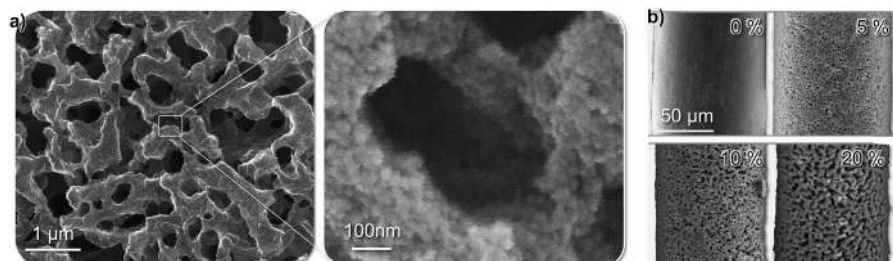


Figure 6.6 Scanning electron microscopy characterization of STRIPS bijels. (a) Magnified bijel surface with high magnification inset. (b) Surfaces of fibers fabricated at different ethanol concentrations (vol%) in the continuous water phase. (a) Adapted from ref. 1 with permission from John Wiley and Sons, © 2015 WILEY-VCH Verlag GmbH & Co. KGaA, Weinheim. (b) Reproduced from ref. 2, <https://doi.org/10.1038/s41467-017-01409-3>, under the terms of the CC BY 4.0 license, <http://creativecommons.org/licenses/by/4.0/>.

ternary mixture by means of the surfactant CTAB, in pure water CTAB induces strong aggregation of the silica particles due to loss of surface charge and the attraction between the alkyl chains of CTAB on silica nanoparticles. The particles adhere to each other *via* the hydrophobic effect, similarly to how micelles form from individual CTAB molecules above the critical micelle concentration (CMC). It is well known that the addition of ethanol to water increases the CMC of CTAB due to the reduction of the hydrophobic effect.¹⁶ Similarly, the attraction between CTAB-coated particles is reduced by the addition of ethanol to the water, resulting in bijels with open bicontinuous surface pores that do not contain aggregated silica particle deposits.

As discussed, the high CTAB concentrations employed for STrIPS bijel fibers with bare silica nanoparticles can result in particle aggregation, clogging the surface pores of the fibers at elevated nanoparticle concentrations. After bijel formation, CTAB remains as a residue within the bijel, interfering with potential applications of these multiphasic composite materials. In the following section, we show that directly surface-functionalized silica nanoparticles allow for the stabilization of STrIPS bijels without, or with significantly reduced, CTAB concentration.

6.3.3 Bijel Fabrication With Functionalized Nanoparticles

STrIPS bijels without CTAB or with significantly reduced surfactant concentrations are desirable for potential applications requiring biocompatibility. Alternative to *in situ* surface modification by CTAB, the wetting properties of nanoparticles can be controlled *via* direct surface functionalization. Metal oxide nanoparticles enable straightforward covalent functionalization with organosilanes. The large library of silanes with different chemical moieties allows attaching almost any functional group to the oxide surface. Moreover, the extent of silanization can be reproducibly controlled by the amount of silane reagent introduced during the functionalization reaction. In the following, we show that silica functionalized with silanes bearing acrylate groups enables the formation of CTAB-free STrIPS bijels.¹⁷

Silica nanoparticles are functionalized with 3-(trimethoxysilyl)propyl acrylate (TPA) to generate partially hydrophobic acrylated silica nanoparticles (ASNPs). The surface coverage of the functional groups is controlled by adding calculated volumes of the organosilanes to a reaction vessel. In the following, we designate particles with different percentages of functionalized silanol groups as 20%-ASNP, 40%-ASNP and 60%-ASNP.

The functionalized particles are added to a ternary mixture comprising water, ethanol and 1,4-butanediol diacrylate (BDA), and STrIPS is carried out. Three-dimensional confocal reconstructions of bijel fiber sections reveal the hierarchical and asymmetric morphology of the ASNP-STrIPS bijels (Figure 6.7a). With increasing percentage of acrylate functionalization, the

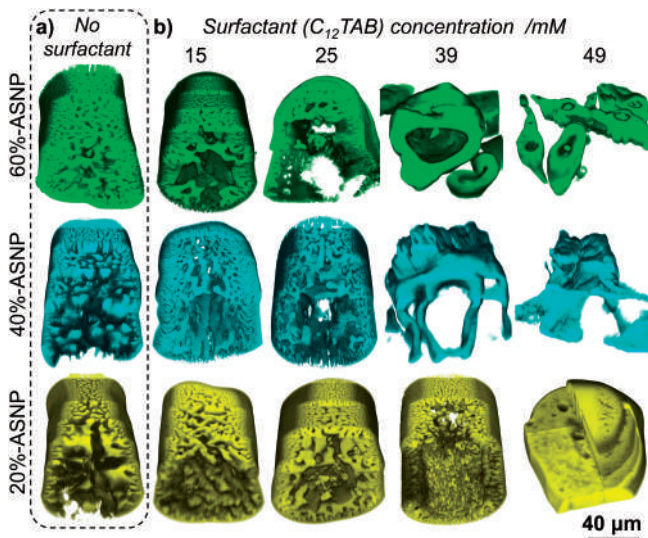


Figure 6.7 STrIPS bijel fabrication with functionalized particles. (a) 3D confocal laser-scanning microscopy reconstructions of STrIPS bijel fibers made solely with ASNPs. The fibers have asymmetric pore size distributions, with small surface pores ($\sim 1.5 \mu\text{m}$) and larger interior oil domains ($\sim 11 \mu\text{m}$). (b) Effect of surfactant concentration on the formation of STrIPS bijels made with ASNPs. Adapted from ref. 17 with permission from the Royal Society of Chemistry.

overall surface area increases, and the surface pore size decreases. However, without polymerizing of the ASNP-stabilized bijels, coarsening takes place over the course of minutes to tens of minutes. The bijels stabilized with 60%-ASNP are the most stable (~ 15 min) followed by 40%-ASNP (~ 6 min) and, lastly, 20%-ASNP (~ 3 min).¹⁷

Long-term stability of the ASNP-STRIPS bijels is realized when cationic surfactants are introduced into the ternary mixture. However, compared with STrIPS bijels formed with bare silica particles, ASNP-stabilized STrIPS bijels require shorter hydrocarbon chain surfactants at lower concentrations for stability. Dodecyl trimethylammonium bromide (C_{12}TAB) allows for the formation of stable structures with structural tunability as shown in Figure 6.7b. Interestingly, a threshold concentration for C_{12}TAB exists, above which bijel structures cannot be formed. This threshold depends on the percentage of functionalization by acrylate groups. The 60%-ASNPs, generate well-defined bijels up to 15 mM C_{12}TAB , while 20%-ASNP form bijels up to 39 mM. Beyond this surfactant threshold, the particles become too hydrophobic, leading instead to the stabilization of water-in-oil emulsions.¹⁷

Besides imparting hydrophobicity, attaching functional groups to the silica particles can introduce additional features, ranging from catalytic properties to sites for nanoparticle cross-linking. We demonstrate the latter by

attaching glycerol groups (3-glycidoxypropyltrimethoxysilane) *via* silanization to the particle surface. In contrast to acrylate-functionalized particles, glycerol functionalization renders the particles hydrophilic, requiring strongly hydrophobic surfactants for bijel stabilization. Addition of didodecyldimethylammonium bromide ($(C_{12})_2TAB$) to the ternary mixture allows for stable bijels that can be reinforced by cross-linking.¹⁷

Tolylene 2,4-diisocyanate-terminated poly (propylene glycol) (TDPPO) is added to the initial ternary mixture containing the glycerol particles. The isocyanate groups in the TDPPO cross-linker react with the terminal hydroxyl groups on the glycerated silica nanoparticles (GSNPs), resulting in cross-linking of the interfacially jammed particles. The cross-linked bijels can withstand elevated pH values. Confocal microscopy shows that adding sodium hydroxide to the surrounding water of a regular bijel results in rapid coarsening of the bicontinuous oil/water scaffold (see Figure 6.10a). On the other hand, the cross-linked bijels are stable after NaOH addition.¹⁷

Cross-linking of the interfacial nanoparticles has enhanced the stability of STrIPS bijels. To realize potential applications of bijel fibers, the mechanical properties need to be tailored. To this end, the means to quantify these properties are needed. The following section introduces a microfluidic *in situ* technique for measurement of the yield strength of the STrIPS bijel fiber.

6.3.4 *In situ* Mechanical Testing of Bijel Fibers

The viscoelastic properties of bijels formed by binary phase separation can be quantified in a parallel plate shear rheometer (see Chapter 2). While spinodal decomposition and interfacial jamming take place, both storage and loss moduli increase.¹⁸ However, at later stages of bijel formation, the storage modulus exceeds the loss modulus by an order of magnitude. Bijels show solid-like material properties, an important assumption for the following analysis.

Conventional rheometers characterize the viscoelastic properties of bulk materials. However, STrIPS bijels cannot be combined with these instruments due to their discrete fiber morphology. However, the hydrodynamic forces within the microfluidic extrusion device can be analyzed to determine the mechanical properties of STrIPS bijels.⁵

As shown in Figure 6.4d, the extrusion of the nanoparticle-doped ternary mixture generates a viscoelastic fiber. Interestingly, the fiber snaps into segments upon increasing the water flow rate around the fiber (Figure 6.8a). The length of these segments decreases with increasing water flow rate. This phenomenon is fundamentally different from the extrusion of pure oil into a stream of an aqueous surfactant solution, for which an increasing water flow rate results in jetting due to high capillary numbers (shear stress to surface tension force ratio). The different extrusion behavior of bijel fibers highlights their viscoelastic character.

Bijel formation within the fiber occurs during translation away from the nozzle. This process results in light scattering by the fiber due to the

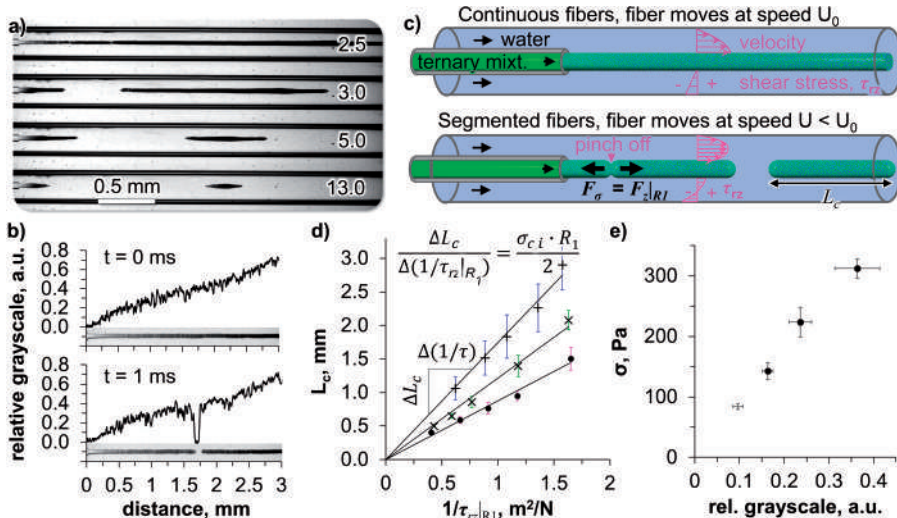


Figure 6.8 Hydrodynamic analysis of bijel fiber segment pinch-off. (a) Micrographs of fiber pinch-off with increasing water flow rate in ml h^{-1} . (b) Measured relative grayscale values of fibers *versus* distance from nozzle. Above the horizontal axes, micrographs of the fiber extrusion are shown. (c) Schematics of fiber extrusion depicting water velocity and shear stress profiles in the annular ring around the fiber (in pink), as well as the force balance during fiber segment pinch-off (in black). (d) Fiber segment length L_c plotted against inverse shear stress on the fiber surface for different relative grayscale values (\bullet , 0.1; \times , 0.15; $+$, 0.24). (e) Yield strength of fibers during pinch-off for different relative grayscale values. Adapted from ref. 5 with permission from American Chemical Society, Copyright 2016.

formation of oil/water/nanoparticle structures. The fiber appears darker with increasing distance from the nozzle (Figure 6.8b). The relative grayscale is defined as the grayscale of the fiber normalized by the final grayscale value. This value represents the stage of bijel formation, with 0 the initial and 1 the final stage. Fiber snapping occurs at characteristic relative grayscale values and is analyzed as follows.

The force that snaps the fiber is the integral over the fiber surface area of the shear stress on the fiber surface $\tau_{rz}|_{R_1}$.⁵ To determine $\tau_{rz}|_{R_1}$, the Navier-Stokes equation for the annular water flow region between the fiber and the outer cylindrical wall is solved. Approximating the fiber as a solid cylinder, the force on the fiber surface is

$$F_z|_{R_1} = \tau_{rz}|_{R_1} 2\pi R_1 L_c$$

where L_c is the length of the snapped fiber segment (Figure 6.8a). While the fiber length L grows during extrusion, the force on the fiber increases due to the increasing area exposed to the shear flow $2\pi R_1 L$. Fiber snapping occurs at the instant that the force within the fiber F_σ and the force resulting from shear stress $F_z|_{R_1}$ are equal, giving

$$F_\sigma = F_z \Big|_{R_1} = \pi R_1^2 \sigma_{c,i} = 2\pi R_1 L_c \tau_{rz} \Big|_{R_1}$$

where $\sigma_{c,i}$ is the yield strength or tensile strength of the fiber. Rearranging this equation for L_c reveals a linear relationship with dependence on $1/\tau_{rz}/R_1$. Figure 6.8d shows plots of L_c against $1/\tau_{rz}/R_1$ for different relative grayscale values. The linear trends suggest that the simple model represents a good approximation for quantifying the tensile strength of the phase-separating fiber. $\sigma_{c,i}$ can be measured from the linear slope. Figure 6.8e plots $\sigma_{c,i}$ against the relative grayscale value, showing an increase of $\sigma_{c,i}$ with increasing phase separation, reflecting the increasing storage modulus of the material.

Measuring $\sigma_{c,i}$ during fiber pinch-off provides information about the bijel formation process, but it does not allow the measurement of the final bijel yield strength, $\sigma_{c,f}$ since fiber snapping always occurs for relative grayscale values < 1 (*i.e.*, when the bijel morphology has not fully developed). However, $\sigma_{c,f}$ can be determined by snapping fiber segments in a microfluidic constriction placed downstream in the bijel formation device, as shown in the following discussion.⁵

A fiber segment is formed and goes through bijel formation during its translation for several centimeters in the cylindrical channel. The segment then enters a microfluidic constriction where strong shear stresses on the fiber result in fiber rupture (Figure 6.9a). The increased velocity of the water in the constriction also accelerates the segment. Rupture takes place when the segment speed reaches a maximum (Figure 6.9b). This motion of the fiber segment results in a remarkable shear stress

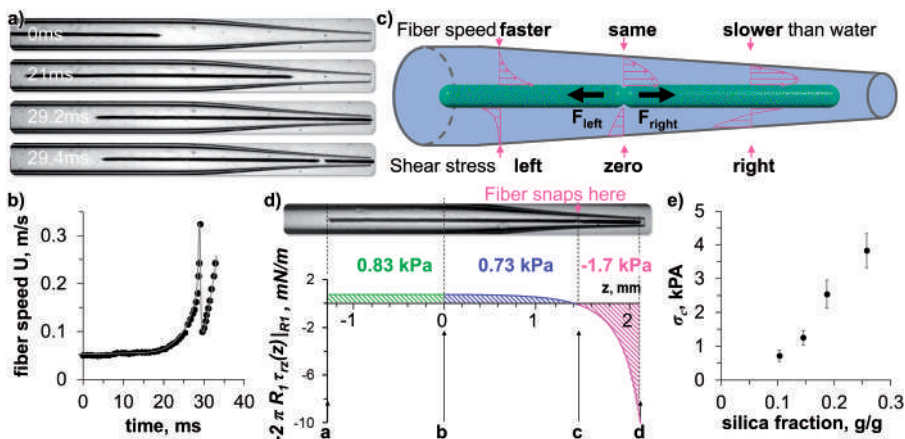


Figure 6.9 *In situ* tensile testing of the final STRIPS bijel material. (a) High speed microscopy of a fiber segment with relative grayscale 1 snapping in microfluidic constriction. (b) The corresponding speed of the fiber segment. (c) Schematics of water velocity and shear stress profile during fiber snapping. (d) Calculation of forces on fiber surface during snapping, (e) Yield strength of fibers with different initial nanoparticle loadings. Adapted from ref. 5 with permission from American Chemical Society, Copyright 2016.

distribution on the fiber surface. A solution of the Navier–Stokes equation for the tapered flow geometry can be obtained based on the lubrication approximation.

Figure 6.9c illustrates the velocity and shear stress distribution around the fiber during rupture. In the narrow section of the constriction, the water moves faster than the fiber, resulting in a positive shear stress that drags the segment into the constriction. However, the water moves slower around the trailing end of the segment due to the fiber acceleration. As a result, a negative shear stress acts on the fiber surface, pulling the fiber backwards.

We split the fiber segment into three regions, a–b: cylindrical part of the capillary, b–c tapered part with negative shear stress, c–d: tapered part with positive shear stress (Figure 6.9d). The shear stresses are integrated over the length of the fiber, resulting in the forces F_{Left} , pulling in the negative z -direction, and F_{right} , pulling in the positive z -direction. The total force on the fiber is calculated by

$$\pi R_1^2 \sigma_{c,f} = F_{\text{Right}} - F_{\text{Left}} = 2\pi \left(\int_a^b R_1(z) \tau_{rz} \Big|_{R_1} dz + \int_b^c R_1(z) \tau_{rz} \Big|_{R_1} dz \right) - 2\pi \left(\int_c^d R_1(z) \tau_{rz} \Big|_{R_1} dz \right)$$

From this balance, we can infer the fracture strength of the fiber $\sigma_{c,f}$ depends strongly on the wt% of silica nanoparticles in the original ternary mixture, ranging from a few hundred Pa at 10 wt% silica particles, up to 4000 Pa (comparable to calcium cross-linked alginate hydrogel) at 25 wt% silica particles (Figure 6.9e). We attribute this increase to the increased number of coagulated silica particles, most likely adhering to each other *via* various attractive interactions such as van der Waals, hydrophobic interactions and capillary forces.

The control of the structure, stability and mechanical properties of STrIPS bijels is important for potential applications of these materials. Bijels have been suggested as innovative materials in food technology, energy storage, separations, catalysis and healthcare (see also Chapter 2). For STrIPS bijels, two applications have been envisioned in the recent literature: (1) reactive separations for chemical reactions between immiscible reagents, and (2) nanocomposite separation membranes for water and organic solvent filtration. To realize both application potentials, unique bijel post-processing steps have been introduced, which are discussed in the next section.

6.4 Biphasic Transport Processes in STrIPS Bijels

6.4.1 Reactive Separations

Biphasic systems represent a versatile reaction medium, given the coexistence of oil and aqueous domains, which allow simultaneous handling of water- and oil-soluble reagents and products, simple separation based

on phase affinity and significantly enhanced reaction kinetics *via* LeChatelier's principle.^{19–27} Simultaneous reactive separation in biphasic liquid media has already been successfully demonstrated to separate reagents and products of differing polarity using Pickering emulsions.^{28–32} However, conventional Pickering emulsions have non-ideal characteristics that limit their potential as microreactors. Although the continuous phase of the Pickering emulsion allows direct addition or removal of reagents, the same is not true for the dispersed phase. It is extremely challenging to continuously supply reagent or to retrieve products from the dispersed phase without costly or complicated separation steps. Furthermore, a higher energy is required to produce Pickering emulsions with high surface areas. Thus, the discrete nature of the droplet phase significantly impedes the development of continuous biphasic reactive separation processes.

Bijels have the potential to circumvent the limitations of conventional Pickering emulsions by enabling continuous operation of biphasic reactive separations.^{33–37} Reagents can be added through one phase, undergo reaction *via* either homogeneous or heterogeneous catalysis and, simultaneously, the product will partition into the other phase. In principle, by feeding one phase with a reactant, and removing the product from the other phase, these systems could operate continuously. Given that many chemical reactions involve vigorous agitation as well as harsh chemical (*e.g.*, high or low pH) and thermal (*e.g.*, high temperature) environments, bijel-based continuous reactive separation can only be enabled if bijels are able to withstand such environments, by possessing mechanical, thermal and/or chemical stability. In the case of as-synthesized bijels, formed by conventional or STrIPS processes, interfacial particles are held together only by weak van der Waals forces, which makes the bijel potentially unsuitable for the reactive environments typical of industrially relevant reactions.

Although the attachment energy of nanoparticles to interfaces can be very large compared with surfactant-stabilized emulsions,³⁸ their surface chemistry and thus their wetting property can change when the chemical environment changes (*e.g.*, pH change). Such a change could potentially induce loss of the bicontinuous morphology or even detachment of nanoparticles from the interface.³⁹ For example, in Figure 6.10a, the bicontinuous morphology of a STrIPS bijel stabilized by CTAB-modified silica nanoparticles transforms into a structure with discrete domains of water in oil when the solution pH is increased from its original value of 3 to a final value of 12. Moreover, STrIPS bijel fibers lose their structural integrity when they are subjected to vigorous stirring, which would pose additional challenges in their use in reactive separation. This chemical and mechanical fragility restricts the potential for application of bijels in reactive separations to a very few chemical reactions that do not necessitate significant environmental changes.

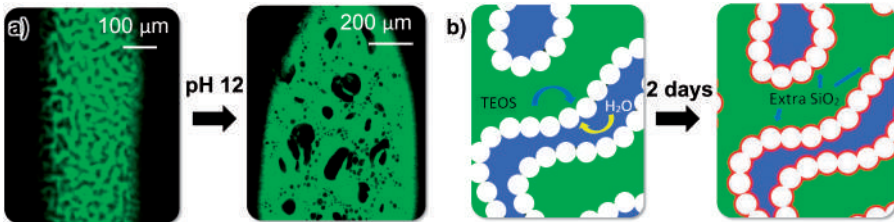


Figure 6.10 Reinforcement of STrIPS bijels. (a) pH change leads to the loss of bicontinuous morphology for non-reinforced STrIPS bijel. (b) Silica-reinforced bijel formation schematics. Tetraethyl orthosilicate (TEOS) partitions in the oil phase upon phase separation and reacts with the surrounding water to create silicon–oxygen covalent bonds that interfacially lock the silica nanoparticles. Fibers are stored for two days to ensure complete TEOS conversion. Adapted from ref. 3 with permission from American Chemical Society, Copyright 2019.

6.4.2 Reinforcement of Bijels for Reactive Separations

Our recent work has shown that such challenges can be overcome by using a sol-gel reaction to covalently bind the silica nanoparticles to each other, thus creating a silica percolating network. This scheme was inspired by previous studies that have reinforced the nanoparticle layers surrounding Pickering emulsion droplets using a silane agent (tetraethyl orthosilicate (TEOS)).^{40,41} To reinforce the interfacially jammed silica nanoparticles in STrIPS bijels, TEOS is added to the ternary mixture. Upon phase separation, TEOS partitions into the bijel's oil phase and reacts with the surrounding water to generate extra silica that binds the nanoparticles to each other, locking them in place in the jammed interfacial layer, as shown schematically in Figure 6.10b. These newly formed covalent bonds prevent the silica nanoparticles from undergoing rearrangement, even if the chemical environment is changed. The reinforced STrIPS bijels maintain their morphology upon pH change, and the fibers do not disintegrate under vigorous stirring. The mechanical properties of the reinforced bijel can be further assessed by removing the two fluid phases by washing the fibers with ethanol multiple times. After drying, the remaining silica scaffold maintains its structure. This is remarkable, as there are significant capillary stresses during the ethanol evaporation. This indicates that the silica network is continuous throughout the entire fiber, and that these reinforced structures have excellent mechanical properties.

6.4.3 Homogeneous Catalysis at High pH

The enhanced mechanical and chemical properties of the reinforced STrIPS bijels enables their use in reactive separation environments that require changes in the solution conditions. Base-catalyzed hydrolysis of ethyl

acetate was chosen as a model reaction to demonstrate that reinforced bijel can be used as a biphasic reaction medium. This type of homogeneous reaction is often performed in the chemical industry. To avoid any decomposition of the oil phase, an inert mixture of cyclohexanone and bromobenzene is chosen as the oil. The reagent, ethyl acetate, is introduced in the ternary mixture, together with TEOS. Upon phase separation, the reagent and TEOS partition into the oil phase. The catalyst (NaOH) is introduced into the aqueous phase to trigger the hydrolysis and condensation of TEOS. Subsequently bijel fibers within a vial are heated for 2 days in an oil bath at 40 °C to induce the hydrolysis of ethyl acetate, as shown in Figure 6.11a.

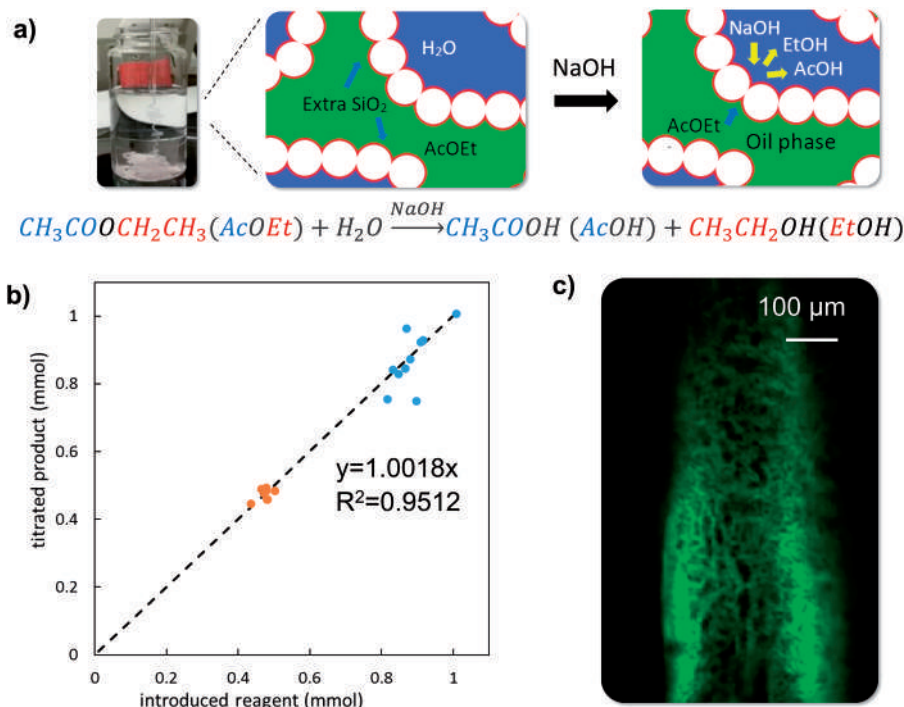


Figure 6.11 Reactive separation in STrIPS bijels. (a) Reactive separation with homogeneous catalyst in STrIPS bijel fiber. The ternary mixture is kept at 0 °C to avoid any unwanted reaction prior to bijel formation. The reagent is loaded in the ternary mixture and upon phase separation partitions in the oil phase, after 2 days the solution pH is increased to the reaction value and the fibers are placed in an oil bath at 40 °C for 2 more days. (b) Product measured by titration against reagent introduced, their ratio equals the ratio between the product and reagent stoichiometric coefficients, which indicates total conversion has been achieved. Blue markers represent reactions performed with a starting pH of 13.5, whereas the orange markers represent reactions performed with a starting pH of 13. (c) Confocal image of bijel fiber after reaction, which shows morphology retention. Adapted from ref. 3 with permission from American Chemical Society, Copyright 2019.

The solution pH of the aqueous phase is reduced due to the release of acetic acid from the hydrolysis reaction (see reaction equation in Figure 6.11a). The extent of reaction can be quantified by titration, which shows that the ratio of product and reagent equals the stoichiometric coefficients ratio. This indicates complete conversion and recovery of the products, as shown in Figure 6.11b. More importantly, the high pH reaction environment did not disrupt the bicontinuous morphology of the reinforced STrIPS bijel, as shown in Figure 6.11c.

6.4.4 Enzymatic Reactive Separations

One of the most important classes of homogeneously catalyzed reactions is enzymatic reactions. A number of enzymatic reactions involve converting highly insoluble substrates into hydrophilic species. For example, the lipase breaks down highly oily substrates into water-soluble species, which is of great industrial importance. Despite their utility, the incompatibility of enzymes with the oily media, and the insolubility of the substrates in the aqueous media, renders these enzymatic reactions inefficient. A recent study has successfully shown that STrIPS bijels can be used as biphasic media that enable reactive separations.⁴² A highly water-insoluble tributyrin was induced to undergo hydrolysis in STrIPS bijels that had lipase in the aqueous domains. In a batch-mode reactive separation scheme, STrIPS bijels increased the initial reaction rate by fourfold compared with the stirred biphasic media. This work demonstrates that bijels can potentially be used as reaction media to enable continuous reactive separations involving biphasic enzymatic reactions.

6.5 Hollow-fiber Membranes

6.5.1 Fabrication of STrIPS Membranes

Separation processes account for up to 15% of the world's total energy consumption.⁴³ Applied to the United States alone, energy-efficient separations could save up to 100 million tons of CO₂ emissions and US\$4 billion annually. Membrane separations are promising alternatives to thermal separations because they do not rely on energy-intensive phase-change operations. Moreover, they are scalable and can be applied to mixtures containing thermally sensitive materials. Developing new membranes requires optimization of cost and scalability, chemical and thermal stability, selectivity and permeability. Advanced membranes need to separate multicomponent mixtures, be resistant to fouling and have high mechanical and chemical stability.

Nanocomposite membranes composed of mixtures of nanoparticles and polymers have many of these attributes, making them attractive for a variety of applications. Their hydrophilicity,⁴⁴ porosity,⁴⁵ charge density,⁴⁶ thermal

and mechanical stability⁴⁷ can be controlled based on nanoparticles with specific functionalities. Moreover, nanocomposite membranes can provide unique features such as antibacterial,⁴⁸ photocatalytic⁴⁹ or adsorptive capabilities.⁵⁰ For instance, microporous zeolites can enhance membrane fluxes at high selectivity for molecular separations.⁵¹ Silver or copper nanoparticles can introduce antimicrobial surface properties to membranes.⁵² The photocatalytic properties of titanium dioxide nanoparticles can introduce self-cleansing of membranes and facilitate the degradation of organic pollutants.³¹

In this section, we describe an approach for the fabrication of nanocomposite membranes that facilitates previously unattainable nanoparticle loadings in membranes and enables the single-step fabrication of nanocomposite membranes composed of highly cross-linked polymers (here, polyacrylates) with pronounced chemical resistance.²

STrIPS bijels are used to template nanocomposite membranes by tailoring their shape into hollow fibers and planar sheets. Figure 6.12 summarizes the fabrication routes to obtain tubular or planar STrIPS bijels. Tubular STrIPS bijels are obtained by coaxial extrusion of water and a stream of the ternary mixture containing a monomeric oil phase into a third stream of water (Figure 6.12a(i)). Phase separation occurs within a cylindrical annulus. The solvent diffuses into both the inner and outer water streams. The hollow fiber translates over a distance long enough to complete phase separation and interfacial jamming (stages 1–3), which is accomplished *via* a scalable mass production route for hollow fibers by collecting the fibers in a water-filled rotating cylinder (Figure 6.12a(ii)). After completion of

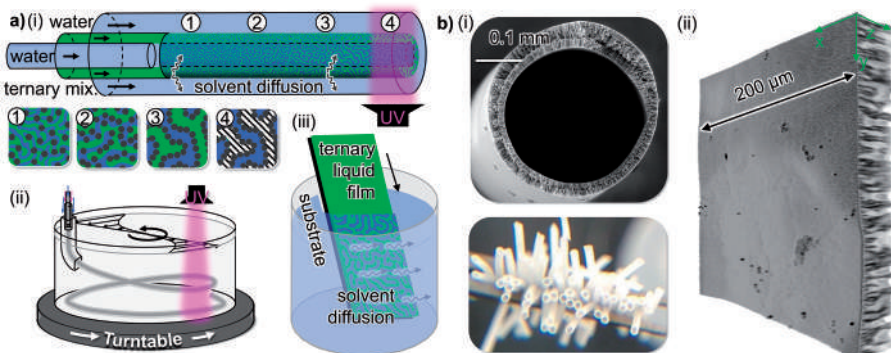


Figure 6.12 Membrane fabrication *via* STrIPS. (a) (i) Schematic of hollow-fiber membrane fabrication, (ii) schematic of straight-fiber collection on turntable, (iii) schematic of planar-membrane fabrication. (b) (i) Electron micrograph and photograph of hollow-fiber membranes and (ii) confocal microscopy 3D reconstruction of planar membrane. Adapted from ref. 2, <https://doi.org/10.1038/s41467-017-01409-3>, under the terms of the CC BY 4.0 license, <http://creativecommons.org/licenses/by/4.0/>.

STrIPS, irradiation with UV light initiates polymerization of the monomeric oil phase and results in a nanocomposite hollow-fiber membrane (stage 4, Figure 6.12a(i)). Alternatively, planar STrIPS bijel membranes are obtained by coating a substrate with a thin film of the ternary mixture and subsequently submerging the film into water (Figure 6.12a(iii)). The resulting hollow fiber and planar membranes are shown in Figure 6.12b.

6.5.2 Structure of STrIPS Membranes

The membrane-formation dynamics can be investigated by arresting intermediate stages of STrIPS *via in situ* polymerization. To this end, the translating fiber is irradiated with high intensity UV light at different distances from the extrusion nozzle (Figure 6.13a). Scanning electron microscopy of fibers polymerized at 5 cm, 15 cm and 30 cm travelling distance shows distinct internal structures (Figure 6.13a(i)). At 5 cm, radially aligned channels (color coded in green) begin growing from the two surfaces of the hollow fiber (see also Figure 6.13b(i)). At 15 cm the channels grow further into the membrane until, at 30 cm, they reach a maximum depth. Between the radially aligned channels, an isotropic granular structure is observed (color coded in blue). Interestingly, the same granular structure results from UV polymerization of a homogeneous ternary mixture (Figure 6.13b(ii)). This finding shows that the region between the radially aligned channels at 5 and 15 cm is composed of a homogeneous ternary liquid mixture. However, at 30 cm the region between the radially aligned channels turns into

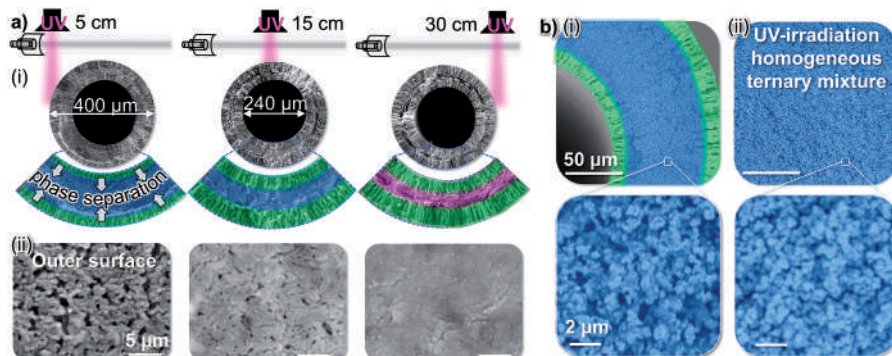


Figure 6.13 Formation processes of STrIPS membranes. (a) Schematics of *in situ* polymerization of STrIPS hollow-fiber membranes. False-colored electron micrographs showing: (i) cross-sectional and (ii) surface perspectives of intermediate stages of the membrane-formation process. (b) Electron micrographs showing a magnified perspective of: (i) the internal structure of a fiber polymerized at 5 cm distance, and (ii) the structure of a UV-polymerized homogeneous ternary mixture. Adapted from ref. 2, <https://doi.org/10.1038/s41467-017-01409-3>, under the terms of the CC BY 4.0 license, <http://creativecommons.org/licenses/by/4.0/>.

an isotropic macroporous structure (color coded in pink, Figure 6.13a(i)), indicating complete phase separation *via* a different mechanism than for the radially aligned structures.

The outer surface of the fiber undergoes a remarkable transformation during fiber translation, with important implications for the selectivity of the membrane during separation applications. At 5 cm travelling distance a nodular structure is observed, reminiscent of spinodal decomposition. However, after 15 cm travelling distance the pore size decreases, until at 30 cm the micrometer-sized surface pores completely disappear. High magnification of the surface at 30 cm distance shows that the entire surface is coated with silica nanoparticles (Figure 6.13a(ii)). We hypothesize that during STrIPS, excess nanoparticles from the internal annular fiber region are transported into the surface pores by the solvent, where they aggregate and deposit as pore fillers.

6.5.3 Features of STrIPS Membranes

The surface pore size for STrIPS membranes ranges from several micrometers to a few nanometers (Figure 6.6b and 6.13a(ii)). This wide range of pore sizes has potential for micro- and ultrafiltration. For STrIPS membranes with defect-free nanoparticle coatings on the surface, the pore size is given by the interstitial spaces between the nanoparticles. With a nanoparticle size of ~20 nm, the size of the interstitial spaces is typically <10 nm, suitable for ultrafiltration.²

To test their separation properties, STrIPS hollow-fiber membranes were assembled into flux-testing devices as shown in Figure 6.14a. After membrane formation, excess CTAB is removed from the membranes by three consecutive washings in a 50/50 (v/v) mixture of 1 mol l⁻¹ HCl and ethanol, each for a period of 6 hours. After rinsing with a copious amount of water, the membranes are dried and assembled on glass slides. Epoxy glue compartmentalizes the fibers into three chambers. Inlets and outlets for feed and filtrate are connected to the respective chambers. The pressurized feed enters the central compartment to permeate into the membrane from the shell side and filtrate drains from the fiber ends. By varying the feed pressure and simultaneously measuring the filtrate mass flow rate, the hydraulic permeability is determined.

The permeability can be controlled over three orders of magnitude by varying the nanoparticle weight fraction within the fiber.² All STrIPS membranes show a linear relationship between the flux (in l (h⁻¹ m⁻²)) and the transmembrane pressure. The slope of the linear fits corresponds to the hydraulic permeability. The hydraulic permeability decreases from 3000 l (h⁻¹ bar⁻¹ m⁻²) to 70 l (h⁻¹ bar⁻¹ m⁻²) by increasing the nanoparticle loading in the membranes from 17 g_{silica}/g_{dry-fiber} to 35 g_{silica}/g_{dry-fiber} (Figure 6.14a). This sharp drop likely results from the increasing mass of silica particles deposited into the pores on the bijel surface (Figure 6.6b and 6.13a(ii)).

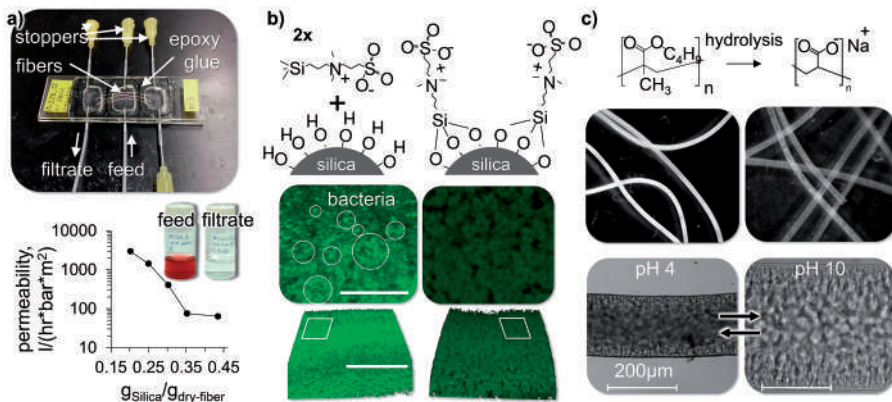


Figure 6.14 STrIPS membrane features. (a) Photograph of flux-testing device and hydraulic permeability dependence on silica nanoparticle fraction in the membranes. Inset: photographs of gold nanoparticle dispersion before/after separation. (b) Schematics of membrane-surface functionalization with zwitterionic silanes and fluorescence micrographs of bare membrane *versus* functionalized membrane after exposure to bacteria suspension. (c) Formation of hydrogel membranes by hydrolysis of polybutylacrylate membrane to polyacrylic acid. Adapted from ref. 2, <https://doi.org/10.1038/s41467-017-01409-3>, under the terms of the CC BY 4.0 license, <http://creativecommons.org/licenses/by/4.0/>.

Gold nanoparticles of 15 nm diameter can be filtered from an aqueous dispersion by STrIPS membranes prepared with 0.35 $\text{g}_{\text{silica}}/\text{g}_{\text{dry-fiber}}$ (Figure 6.14a (inset)).² In contrast, nanoparticles cannot be separated by membranes prepared with $<0.35 \text{ g}_{\text{silica}}/\text{g}_{\text{dry-fiber}}$. This finding highlights the potential applications of STrIPS membranes for separations. Future research is aimed at further reducing the surface pore size of the membranes for higher selectivities, for instance *via* post-functionalization of the membrane surface *via* the methods described earlier in Section 6.5.

Additional features of the membranes can be derived from the nanoparticle and polymer constituents. For instance, the silanol groups on the silica nanoparticles allow for straightforward surface functionalization of the membranes. Here, we show that silanization with a zwitterionic silane (sulfo-betaine silane, SbSi) reduces bacterial biofouling on the membrane surface. SbSi-functionalized membranes do not show fluorescent bacteria deposition after 24 hours exposure, while untreated membranes show bacteria growth on the surface (Figure 6.14b).

Furthermore, selecting different monomers can introduce more features to STrIPS bijel membranes. Addition of difunctional acrylate monomers, such as hexanedioildiacrylate or butanedioildiacrylate, results in highly cross-linked polymer backbones that allow for membrane stability in organic solvents. This opens potential applications for organic solvent filtration.

Moreover, membranes formed with the tertiary butyl acrylate can be converted into stimuli-responsive hydrogel membranes. To this end, poly(*tert*-butylacrylate) in a STrIPS membrane is converted to poly(acrylic acid) by hydrolysis (Figure 6.14c). This membrane swells dramatically by increasing the pH value of the aqueous media. The resulting hydrogel scaffolds have potential applications as stimuli-responsive membranes that can open/close their pores on demand.

6.6 Outlook and Future Perspectives

Ongoing and future research on STrIPS bijels is driven by the demands to further understand the colloidal stability in the ternary mixture, to identify the underlying processes occurring during STrIPS, to tailor and measure mechanical properties, as well as to explore the applications of STrIPS bijels. In this section we discuss the basic research needs for STrIPS, followed by a discussion of the potential directions for promoting applications of STrIPS bijels.

6.6.1 Future Research to Determine General Principles of STrIPS Bijel Formation

An important basic research need concerns the formation of STrIPS bijels with nanoparticles other than silica. To this end, studies of the surfactant-nanoparticle interactions are required (see Chapter 7) to establish general principles for particle dispersion in ternary mixtures, as well as bijel stabilization. Alternatively, covalent surface modifications of nanoparticles for STrIPS bijel stabilization can be investigated. An unexplored research direction is to investigate the effect of nanoparticle size⁵³ and polydispersity on STrIPS bijel structures. Also, the use of particles of different shapes, for instance high aspect ratio colloids or platelets, will result in interesting effects for STrIPS bijels.^{54,55} Last, the use of amphiphilic Janus particles can also be investigated for STrIPS bijel formation, potentially allowing for the formation of periodic structures.⁵⁶

Fundamental studies determining the formation principles of the oil/water scaffold of STrIPS bijels are needed to tailor bijel structures. For instance, STrIPS bijels intended as separation membranes require small surface pores for size selective separations and a porous and bulky membrane substructure for mechanical support. In contrast, STrIPS bijels tailored for biphasic reactive separations require an open surface pore structure enabling unobstructed transport of reagents and products in and out of the bijel structure. Moreover, a large internal surface area is needed to enable efficient biphasic mass transfer. To this end, more fundamental research will show how to fabricate STrIPS bijels with uniform bicontinuous domains, a feature that has until now only been observed for bijels formed by binary phase separation. To realize this goal, the relationship between structure and mass transfer

needs to be investigated further. Moreover, the role of the ternary liquid phase equilibrium and the partitioning of the solvent between the phases requires further understanding. More research is also needed to connect STrIPS bijel structure with the nanoparticle surface chemistry.

To further understand bijel fiber mechanics and to determine potential applications, other mechanical moduli besides the tensile strength need to be quantified; for instance, the Young's modulus and the bending modulus. The mechanical characterization of bijel fibers fabricated with different ternary liquid compositions is of interest to connect the structure with the material properties. Last, the mechanical properties of reinforced bijel fibers need to be quantified.

Other possibilities for bijel fibers in hydrodynamic flow fields lie in the assembly of fibers into helical structures, such as bundles. For instance, rotational flow fields can allow twisting of multiple parallel bijel fibers into bundles with enhanced mechanical strength. Moreover, 3D printing of fibers will allow controlled assemblies for specific applications, such as reactive separations, discussed in the next section.

6.6.2 Research to Promote Applications of STrIPS Bijels

STrIPS bijels have great potential for simultaneous reaction and separation in continuously operated interfacial catalysis.³² Demonstrating this capability has the potential to initiate the creation of a new research field by integrating biocatalysis,⁵⁷ biofuel²⁸ and specialty chemical synthesis,⁵⁸ as well as drug development and production⁵⁹ in bijels. The potential to continuously flow reactants in, and products out, of STrIPS bijels has been inspired by the observation of fluorescent dye transport *via* molecular diffusion (Figure 6.15a).

Aligned fibers can be connected with oil reservoirs. Figure 6.15a shows the diffusion of a hydrophobic fluorescent dye from the oil reservoir throughout the oil domains of the fibers. Alternatively, adding a hydrophilic fluorescent dye to the external water proves the connectivity between external and internal water domains (Figure 6.15b). Moreover, a dye can undergo phase transfer from water to oil (Figure 6.15b). These experiments demonstrate the potential for biphasic transport, as well as the permeability of the

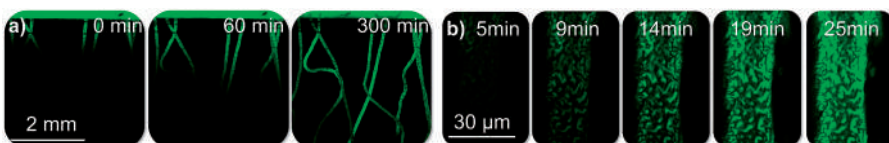


Figure 6.15 Transport in STrIPS bijels. (a) Diffusion of a hydrophobic dye (Nile red) from an oil reservoir (top) across the length of the fiber. (b) Diffusion of Nile red dissolved in aqueous CTAB micelles from water to oil.

interfacially jammed nanoparticle layer. What remains open to question is whether convective biphasic flows can be realized in bijels. This milestone will unlock the full potential of interfacial mass transfer and Pickering interfacial catalysis in bijels.

Reinforcement *via* sol-gel reaction has proven to be a critical step in enabling reactive separation using STrIPS bijels, albeit in a batch fashion and using a homogeneous catalyst. This exciting development brings the community one step closer to realizing the continuous reactive separation that was envisioned with the discovery of bijels. To truly exploit the full potential of bijels in continuous heterogeneous catalyzed reactive separations, several outstanding questions must be addressed.

Heterogeneous catalysis requires either the deposition of catalytic materials onto the interfacially jammed particles or using catalytic materials themselves to induce interfacial jamming, instead of silica nanoparticles. The deposition of catalytic material on silica nanoparticles could be theoretically made before or after STrIPS. Both approaches present important challenges, since surfactants may adsorb on the catalyst reducing its activity; moreover, surface chemistry modification of silica nanoparticles before being used in the STrIPS process may severely affect their stability and wetting properties. These limitations suggest a more robust way of producing bijels without relying on surfactant modification would be necessary.

Reactor design is another challenging aspect, since bijel oil and water domains need to be connected to oil and water reservoirs to supply reagents and withdraw products. Therefore a clever bijel reactor design has to be implemented. Moreover, mass transfer from the oil and water reservoirs to the oil and water compartments of the bijels might strongly limit reactive separation, since diffusion of reagents and products through the nanoparticle layer of bijel domains might be very slow. Previous studies on catalysis on traditional Pickering emulsions have shown that it is possible to develop a biphasic reactor configuration free of mass transfer limitations,³² thus there is a need for a reactor design able to export those features on a bicontinuous Pickering emulsion system.

These advances will enable the use of bijels in relevant industrial and scientific reactive separations, such as the condensation reaction of biomass-derived oxygenates⁶⁰ and formation of oleo-furan surfactants.⁶¹

STrIPS bijel membranes also have the distinct possibility to become scalable ultrafiltration, organic solvent nanofiltration and catalytic membranes. This potential application is feasible since nanoparticle-covered STrIPS bijel membranes enable simple membrane-surface functionalizations, and can be fabricated with cross-linkable monomers and with catalytic nanoparticles. Moreover, they can be readily fabricated in large quantities as hollow-fiber membranes or as flat-sheet membranes. However, before these new types of membranes can be industrially applied, three

advances need to be made: (1) enhancement of the mechanical properties of STrIPS membranes, (2) formation of defect-free nanoparticle coatings on the membranes and (3) enhancing the selectivity of STrIPS membranes for separations.

6.7 Conclusion

In summary, this chapter has introduced bijels formed by solvent transfer-induced phase separation. Complementary to the generation of bijels *via* binary phase separation³⁴ or simple shear emulsification,^{62,63} STrIPS generates bicontinuous particle-stabilized emulsions. However, unique to STrIPS is the continuous production route of bijels in the form of fibers, planar films and microparticles. Moreover, STrIPS bijels have asymmetric architectures, with small bicontinuous surface domains and larger internal domains. The unique structures of STrIPS bijels have enabled the templating of hollow-fiber membranes for ultrafiltration, and the realization of reactive separations in biphasic microreactors. Future research perspectives on STrIPS bijels show great opportunities to advance knowledge on the interplay of ternary liquid–liquid phase separation and interfacial nanoparticle stabilization, as well as the widening of applications for STrIPS bijels as separation membranes and as catalytic microreactors for the continuous production of specialty chemicals, pharmaceuticals and biofuels.

Acknowledgements

The preparation of this chapter has been funded by the European Research Council (ERC) under the European Union's Horizon 2020 research and innovation programme (Grant agreement No. GA802636).

References

1. M. F. Haase, K. J. Stebe and D. Lee, *Adv. Mater.*, 2015, **27**, 7065–7071.
2. M. F. Haase, H. Jeon, N. Hough, J. H. Kim, K. J. Stebe and D. Lee, *Nat. Commun.*, 2017, **8**, 1234.
3. G. Di Vitantonio, T. Wang, M. F. Haase, K. J. Stebe and D. Lee, *ACS Nano*, 2018, **13**, 26–31.
4. M. F. Haase and J. Brujic, *Angew. Chem., Int. Ed.*, 2014, **53**, 11793–11797.
5. M. F. Haase, N. Sharifi-Mood, D. Lee and K. J. Stebe, *ACS Nano*, 2016, **10**, 6338–6344.
6. S. A. Vitale and J. L. Katz, *Langmuir*, 2003, **19**, 4105–4110.
7. C. X. Zhao and A. P. Middelberg, *Angew. Chem., Int. Ed.*, 2009, **48**, 7208–7211.

8. W.-C. Jeong, M. Choi, C. H. Lim and S.-M. Yang, *Lab Chip*, 2012, **12**, 5262–5271.
9. Y. Song and H. C. Shum, *Langmuir*, 2012, **28**, 12054–12059.
10. C. H. Choi, D. A. Weitz and C. S. Lee, *Adv. Mater.*, 2013, **25**, 2536–2541.
11. M. C. Fuerstenau, G. J. Jameson and R. H. Yoon, *Froth flotation: A century of innovation*, Society for Mining, Metallurgy, and Exploration, 2007.
12. L. Tran and M. F. Haase, *Langmuir*, 2019, **35**, 8584–8602.
13. B. P. Binks, J. A. Rodrigues and W. J. Frith, *Langmuir*, 2007, **23**, 3626–3636.
14. B. P. Binks, L. Isa and A. T. Tyowua, *Langmuir*, 2013, **29**(16), 4923–4927.
15. M. F. Haase, Modification of nanoparticle surfaces for emulsion stabilization and encapsulation of active molecules for anti-corrosive coatings, PhD Thesis, University of Potsdam, Potsdam, 2011.
16. C. Tanford, *The Hydrophobic Effect: Formation of Micelles and Biological Membranes*, John Wiley, 2nd edn, 1980.
17. S. Boakye-Ansah, M. S. Schwenger and M. Haase, *Soft Matter*, 2019, **15**, 3379–3388.
18. M. N. Lee, J. H. Thijssen, J. A. Witt, P. S. Clegg and A. Mohraz, *Adv. Funct. Mater.*, 2013, **23**, 417–423.
19. J. Jarrousse, *C. R. Chim.*, 1951, **232**, 1424–1426.
20. E. F. J. G. Duynstee and E. Grunwald, *J. Am. Chem. Soc.*, 1959, **81**, 4540–4542.
21. F. M. Menger, J. A. Donohue and R. F. Williams, *J. Am. Chem. Soc.*, 1973, **95**, 286–288.
22. F. Joó, *Acc. Chem. Res.*, 2002, **35**, 738–745.
23. D. J. Cole-Hamilton, *Science*, 2003, **299**, 1702–1706.
24. K. Manabe, S. Iimura, X.-M. Sun and S. Kobayashi, *J. Am. Chem. Soc.*, 2002, **124**, 11971–11978.
25. P. Tundo and A. Perosa, *Chem. Soc. Rev.*, 2007, **36**, 532–550.
26. S. Minakata and M. Komatsu, *Chem. Rev.*, 2009, **109**, 711–724.
27. X. Yang, X. Wang and J. Qiu, *Appl. Catal., A*, 2010, **382**, 131–137.
28. S. Crossley, J. Faria, M. Shen and D. E. Resasco, *Science*, 2010, **327**, 68–72.
29. J. Faria, M. P. Ruiz and D. E. Resasco, *Adv. Synth. Catal.*, 2010, **352**, 2359–2364.
30. M. P. Ruiz, J. Faria, M. Shen, S. Drexler, T. Prasomsri and D. E. Resasco, *ChemSusChem*, 2011, **4**, 964–974.
31. P. Gao, Z. Liu, M. Tai, D. D. Sun and W. Ng, *Appl. Catal., B*, 2013, **138**, 17–25.
32. M. Zhang, L. Wei, H. Chen, Z. Du, B. P. Binks and H. Yang, *J. Am. Chem. Soc.*, 2016, **138**, 10173–10183.
33. K. Stratford, R. Adhikari, I. Pagonabarraga, J. C. Desplat and M. E. Cates, *Science*, 2005, **309**, 2198–2201.
34. E. M. Herzog, K. A. White, A. B. Schofield, W. C. K. Poon and P. S. Clegg, *Nat. Mater.*, 2007, **6**, 966–971.

35. M. E. Cates and P. S. Clegg, *Soft Matter*, 2008, **4**, 2132.
36. J. W. Tavacoli, J. H. J. Thijssen, A. B. Schofield and P. S. Clegg, *Adv. Funct. Mater.*, 2011, **21**, 2020–2027.
37. M. Reeves, K. Stratford and J. H. J. Thijssen, *Soft Matter*, 2016, **12**, 4082–4092.
38. S. Levine, B. D. Bowen and S. J. Partridge, *Colloids Surf.*, 1989, **38**, 325–343.
39. V. Pouliche and V. Garbin, *Proc. Natl. Acad. Sci. U. S. A.*, 2015, **112**, 5932–5937.
40. Y. Liu, X. Chen and J. H. Xin, *J. Mater. Sci.*, 2006, **41**, 5399–5401.
41. H. Wang, X. Zhu, L. Tsarkova, A. Pich and M. Möller, *ACS Nano*, 2011, **5**, 3937–3942.
42. S. Cha, H. G. Lim, M. F. Haase, K. J. Stebe, G. Y. Jung and D. Lee, *Sci. Rep.*, 2019, **9**, 6363.
43. D. S. Sholl and R. P. Lively, *Nature*, 2016, **532**, 435–437.
44. A. Tiraferri, Y. Kang, E. P. Giannelis and M. Elimelech, *Environ. Sci. Technol.*, 2012, **46**, 11135–11144.
45. Y. Ma, F. Shi, W. Zhao, M. Wu, J. Zhang, J. Ma and C. Gao, *Desalination*, 2012, **303**, 39–47.
46. H. Wu, B. Tang and P. Wu, *J. Membr. Sci.*, 2014, **451**, 94–102.
47. C. H. Worthley, K. T. Constantopoulos, M. Ginic-Markovic, E. Markovic and S. Clarke, *J. Membr. Sci.*, 2013, **431**, 62–71.
48. M. S. Mauter, Y. Wang, K. C. Okemgbo, C. O. Osuji, E. P. Giannelis and M. Elimelech, *ACS Appl. Mater. Interfaces*, 2011, **3**, 2861–2868.
49. H. Ngang, B. Ooi, A. Ahmad and S. Lai, *Chem. Eng. J.*, 2012, **197**, 359–367.
50. R. J. Gohari, W. Lau, T. Matsuura, E. Halakoo and A. Ismail, *Sep. Purif. Technol.*, 2013, **120**, 59–68.
51. M. Y. Jeon, D. Kim, P. Kumar, P. S. Lee, N. Rangnekar, P. Bai, M. Shete, B. Elyassi, H. S. Lee and K. Narasimharao, *Nature*, 2017, **543**, 690.
52. K. Zodrow, L. Brunet, S. Mahendra, D. Li, A. Zhang, Q. Li and P. J. Alvarez, *Water Res.*, 2009, **43**, 715–723.
53. M. Reeves, A. T. Brown, A. B. Schofield, M. E. Cates and J. H. J. Thijssen, *Phys. Rev. E*, 2015, **92**, 032308.
54. N. Huijnen, D. Cai and P. S. Clegg, *Soft Matter*, 2015, **11**, 4351–4355.
55. L. Imperiali, C. Clasen, J. Fransaer, C. W. Macosko and J. Vermant, *Mater. Horiz.*, 2014, **1**, 139–145.
56. A. Krekhov, V. Weith and W. Zimmermann, *Phys. Rev. E*, 2013, **88**, 040302.
57. Z. Wang, M. C. van Oers, F. P. Rutjes and J. C. van Hest, *Angew. Chem., Int. Ed.*, 2012, **51**, 10746–10750.
58. H. Nur, S. Ikeda and B. Ohtani, *J. Catal.*, 2001, **204**, 402–408.
59. F. Lévesque and P. H. Seeberger, *Angew. Chem., Int. Ed.*, 2012, **51**, 1706–1709.
60. P. A. Zapata, J. Faria, M. Pilar Ruiz and D. E. Resasco, *Top. Catal.*, 2012, **55**, 38–52.

61. D. S. Park, K. E. Joseph, M. Koehle, C. Krumm, L. Ren, J. N. Damen, M. H. Shete, H. S. Lee, X. Zuo, B. Lee, W. Fan, D. G. Vlachos, R. F. Lobo, M. Tsapatsis and P. J. Dauenhauer, *ACS Cent. Sci.*, 2016, **2**, 820–824.
62. D. Cai, P. S. Clegg, T. Li, K. A. Rumble and J. W. Tavacoli, *Soft Matter*, 2017, **13**, 4824–4829.
63. C. Huang, J. Forth, W. Wang, K. Hong, G. S. Smith, B. A. Helms and T. P. Russell, *Nat. Nanotechnol.*, 2017, **12**, 1060–1063.